Defects controlling, elements doping, and crystallinity improving triple-strategy modified carbon nitride for efficient photocatalytic diclofenac degradation and H_2O_2 production

Qinglun You [a,b], Chunsheng Zhang [a,b], Min Cao [a], Bin Wang [a,b], Jun Huang [a,b], Yujue Wang [a,b], Shubo Deng [a,b], Gang Yu [a,b,*]

[a] State Key Joint Laboratory of Environmental Simulation and Pollution Control, School of Environment, Tsinghua University, Beijing 100084, China
[b] Beijing Key Laboratory for Emerging Organic Contaminants Control, Beijing Laboratory for Environmental Frontier Technologies, China

A B S T R A C T

The development of an effective dual-function photocatalyst for refractory contaminant abatement and sacrificial-free in-situ H_2O_2 generation is a major challenge. Herein, defects controlling, elements doping, and crystallinity improving triple-strategy is established to synthesize modified g-C_3N_4 (SCBCN$_{0.4}$). The triple-strategy of modification reconciles crystallinity improvement and the decoration of moderate cyano-group defects and B and O co-dopants. Characterization experiments and theoretical calculations reveal microstructure and electronic structure optimization, improved light-harvesting capability, and enhanced carrier separation efficiency. SCBCN$_{0.4}$ performs admirably in the degradation of diclofenac and a variety of other pharmaceuticals. Through synchronous oxygen reduction and water oxidation processes, SCBCN$_{0.4}$ has an excellent in-situ photocatalytic H_2O_2 generation rate of 620 µmol/g/h (309 µmol/g/h without sacrificial agents). SCBCN$_{0.4}$'s detoxification, reusability, and stability were validated in several experiments. Hence, this research offers a ground-breaking approach to manufacturing triple-strategy modified g-C_3N_4 for environmental remediation and (sacrificial-free) in-situ H_2O_2 production.

1. Introduction

Environmental issues and energy crises are significant obstacles to human development that must be overcome. Increasing pharmaceutical pollution of aquatic environments, for example, diclofenac (DCF), has prompted significant concern about its widespread environmental presence and potential risks [1]. DCF residues have been found in the aquatic environment in quantities ranging from ng/L to µg/L as a result of continuous introduction due to extensive consumption [2]. Even at a low concentration, DCF has been reported to interfere with several environmental species, with the detrimental effect amplified by biomagnification and posing a threat to human health [3,4]. However, of multiple factors, conventional wastewater treatment plants as well as general physical and biological methods are ineffective in completely decomposing DCF [5]. Meanwhile, hydrogen peroxide (H_2O_2) has received increasing attention as a clean energy carrier and environmentally friendly oxidant for environmental remediation. H_2O_2 is widely used for activation to generate hydroxyl radicals (·OH) to treat hazardous wastewater, such as Fenton/Fenton-like processes, due to its high oxygen content and no harmful by-products [6]. However, the traditional industrial H_2O_2 production process (anthraquinone oxidation process) consumes significant amounts of energy and generates a lot of waste, and H_2O_2 transportation and storage are insecure [7,8].

Photocatalysis is a sustainable "One-Stone-Two-Birds" process that degrades refractory organic pollutants and converts solar energy into chemical energy (H_2O_2), using water and oxygen as source materials [9]. However, efficient photocatalytic destruction of refractory contaminants is challenging, and eliminating the need for sacrificial agents in efficient H_2O_2 production remains a hurdle [10]. As a result, developing a dual-function photocatalyst for effective DCF abatement and sacrificial-free in-situ H_2O_2 generation is vital; the latter, in particular, is crucial in laying the groundwork for addressing energy needs and further H_2O_2 activation for waste disposal.

In the photocatalysis domain, graphitic carbon nitride (g-C_3N_4)

exhibits great feasibility in environmental remediation and H_2O_2 production due to its superior nature, including visible-light response, "earth-abundant" property, chemical stability, and tunable structure [11]. However, the intrinsic obstacles of g-C_3N_4, such as inefficient light adsorption, low electrical conductivity, and fast recombination of photogenerated carriers, necessitate the further use of appropriate modification strategies [12]. Some general strategies, such as defect decoration and elemental doping, are employed to regulate the composition, electronic structure, redox potential, carrier migration, and reactive sites [13,14]. In particular, cyano-groups ($-C\equiv N$) defects have been identified as exciton dissociation traps and catalytically relevant sites for *OOH formation and subsequent hydrogenation [15,16]. And oxygen and boron doping in the tri-s-triazine structure may facilitate exciton dissociation and lower the thermodynamic and kinetic barriers of H_2O_2 production, concurrently provide electron-deficient and electron-rich environment, and enable charge redistribution [17–20]. However, fabricating defects and introducing dopants can also result in structural imperfections for charge recombination and be incompatible with the objective of enhancing crystallinity and its superior properties, such as thermal stability, charge conductivity, and light-harvesting capacity [21,22]. Therefore, decorating moderate defects and dopants while also increasing crystallinity is conducive to making good use of each strength and optimizing g-C_3N_4 for maximal performance. Developing such balancing strategies continues to be quite challenging.

Herein, defects controlling, elements doping, and crystallinity improving triple-strategy was established through the thermal post-treatment of self-assembled carbon nitride with sodium cyanoborohydride to synthesize modified g-C_3N_4 (SCBCN$_{0.4}$). Combining with experiments and theoretical calculations, this work (i) explores the unique role of the novel post-treatment in reconciling crystallinity improvement and the introduction of defects and dopants, (ii) identifies the microstructure of SCBCN$_{0.4}$ and its optical and electrochemical properties, as well as carriers transfer efficiency, (iii) discusses the photocatalytic performance and mechanism of pharmaceutical degradation and H_2O_2 production, (iv) assesses the detoxification, reusability, and stability of SCBCN$_{0.4}$. This study provides a pioneering perspective for the fabrication of triple-strategy modified g-C_3N_4 for environmental remediation and (sacrificial-free) in-situ H_2O_2 production.

2. Methods and materials

Reagents, (photo)electrochemical measurements, rotating disk electrode measurements, rotating ring-disk electrode measurements, additional measurements of photocatalytic degradation, analytical methods of pharmaceuticals and DCF degradation intermediates, scavenger-quenching experiments and electron paramagnetic resonance tests, theoretical calculations, acute toxicity evaluation, and reusability tests are provided in Text S1, S2, S3, S4, S5, S6, S7, S8, S9, and S10 in Supplementary Material.

2.1. Preparation of photocatalysts

The porous carbon nitride (PCN) was synthesized via a supramolecular self-assembly process based on previous studies [23,24]. Typically, 10 mmol of melamine and 10 mmol of cyanuric acid were dissolved in 60 mL of DI water and stirred for 12 hours. Then, the obtained suspension was centrifuged at 8000 rpm for 10 mins and dried overnight. Finally, the obtained supramolecular precursors were calcined in a tube furnace at 550°C for 4 hours to obtain PCN.

Sodium cyanoborohydride modified carbon nitride (SCBCN$_x$) were fabricated through a thermal post-treatment of PCN. Typically, 0.30 g of PCN and a certain quantity of sodium cyanoborohydride are thoroughly ground before being calcined for 1 hour at 400°C in a nitrogen atmosphere. The obtained solid was washed with DI water and ethanol and then dried overnight. As-prepared photocatalysts were recorded as SCBCN$_x$ (x = 0.2, 0.3, 0.4, 0.5, and 0.6, representing 20%, 30%, 40%,

50%, and 60% weight percentage of sodium cyanoborohydride to PCN). While sodium borohydride modified carbon nitride (SBCN$_x$) (x = 0.3, 0.4, and 0.5) were fabricated under the same conditions except that sodium borohydride replaces sodium cyanoborohydride.

As a comparison, the pure melamine was calcined at 550°C for 4 hours to synthesize the bulk g-C_3N_4. Besides, SBGCN$_{0.4}$ and SCBGCN$_{0.4}$ (0.4 representing 40% weight percentage of sodium borohydride or sodium cyanoborohydride to g-C_3N_4) were prepared based on the methods of SBCN$_{0.4}$ and SCBCN$_{0.4}$ by thermal post-treatment of g-C_3N_4.

2.2. Characterization

The scanning electron microscope (SEM) images and transmission electron microscope (TEM) images were obtained to explore the morphology and microstructure of samples using a JSM-7900F field emission scanning electron microscope (JEOL Ltd., Japan) and a JEM-2100F plus field emission transmission electron microscope (JEOL Ltd., Japan), respectively. And the crystal structures were analyzed through X-ray diffraction (XRD) patterns obtained on a D/max-2550 diffractometer (Rigaku, Japan) with Cu Kα (λ = 1.54059 Å) irradiation at 40 kV and 40 mA. Fourier transform infrared (FT-IR) spectra were recorded using a Nicolet 6700 FTIR spectrometer system (Thermo Fisher, USA). The samples were dried and mixed with KBr before tablet molding. The N_2 adsorption isotherms were measured on an Autosorb iQ3 (Quantachrome, USA) at −196°C, and the samples were evacuated at 300°C for four hours before analyses. Elemental analysis was carried out on a Vario EL II elemental analyzer (Elementar, Germany). X-ray photoelectron spectroscopy (XPS) was collected using an ESCALAB 250Xi X-ray photoelectron spectrometer (Thermo Fisher, UK) with Al-Kα radiation, and all binding energies were set to C1s signal at 284.8 eV for calibration. Solid-state ^{13}C and ^{11}B MAS NMR spectra were obtained by a JNM-ECZ600R NMR spectrometer (JEOL Ltd., Japan). A UV-2700 UV–Vis spectrophotometer (Shimadzu, Japan) was used to record the UV–Vis diffuse reflectance spectra of samples, and the photoluminescence spectra were measured with a Hitachi F-7000 fluorescence spectrophotometer (Hitachi, Japan) with an excitation wavelength of 367 nm. Time-resolved transient fluorescence decay spectra were obtained with the FLSP920 fluorescence spectrometer (Edinburgh, UK) with an excitation wavelength of 367 nm.

2.3. Photocatalytic experiments

2.3.1. Photocatalytic degradation

The degradation of diclofenac and several other pharmaceuticals was conducted in a photochemical reactor (Fig. S1; PCX-50 C Discover, Beijing PerfectLight, China) to assess the performance of obtained samples. For the light source, a 10 W LED lamp with a UV cutoff filter ($\lambda \geq$ 420 nm) was used. Typically, 5 mg of photocatalyst (0.1 g/L) was dispersed in a 50 mL aqueous solution containing the target contaminant (8 mg/L), and the suspension would be stirred for 30 mins before irradiation. To ensure well-mixed conditions, the photocatalytic process was conducted while stirring. The temperature was kept constant at 25.0 ± 0.1°C. 1 mL of the mixture was extracted and filtered at regular intervals and subsequently determined using high-performance liquid chromatography (Agilent Technologies, USA). More measurements of photocatalytic degradation and the detailed analytical methods were conveyed in Text S5, Text S6, and Table S1.

2.3.2. Photocatalytic H_2O_2 production

The photocatalytic activity of H_2O_2 production was carried out in a 100 mL solution (10 vol% ethanol) containing 40 mg of catalysts. Exposed to the visible light irradiation from a PLS-SXE300 xenon lamp (300 W, λ > 420 nm; Beijing PerfectLight, China), the suspension solutions were kept stirred under O_2 equilibrium conditions, and the temperature was controlled at 25.0 ± 0.1°C. A 2 mL suspension was taken and centrifuged at regular intervals for the determination of H_2O_2

concentrations using iodometry. Concretely, samples were mixed with 1 mL of aqueous potassium hydrogen phthalate (0.1 M) and aqueous potassium iodide (0.4 M), and the absorbance at 350 nm was measured by a UV–vis spectrometer (DR6000, HACH, USA) after 30 mins.

3. Results and discussion

3.1. Characterization and theoretical calculations

The morphology and microstructure of as-prepared photocatalysts were revealed in SEM and TEM spectra. Pristine PCN displays a typical bulk-agglomerate and stacked-layered structure (Fig. 1a). In contrast, $SBCN_{0.4}$ shows a broken sheet structure with large pores (Fig. 1c), attributed to strong reductive H_2 derived from $NaBH_4$ attacking the framework of PCN [25]. While $SCBCN_{0.4}$ exhibits locally ordered structure and crystallization (Fig. 1b and e), as evidenced by the distinct lattice fringes observed in HRTEM. The measured lattice fringe is 0.24 nm, indexed to the in-plane d-space of carbon nitride [26]. Furthermore, the diffraction ring observed in the selected area electron diffraction (SAED) reflects a favorable crystallinity of $SCBCN_{0.4}$. In addition, TEM-EDS element mapping was investigated to explore the elemental composition of $SCBCN_{0.4}$. As demonstrated in Fig. S2, $SCBCN_{0.4}$ mainly contains C and N elements, while a few O and B elements are also evenly distributed on $SCBCN_{0.4}$, indicating the possible doping of O and B atoms and almost no sodium residue.

As depicted in X-ray diffraction (XRD) patterns, all samples exhibit two well-defined diffraction peaks at around 13.0° (1 0 0) and 27.6° (0 0 2), representing the in-plane compression of tri-s-triazine units and interlayer stacking, respectively [27]. Consistent with the analyses above, the $NaBH_3CN$-assisted post-treatment improves the interplanar packing and interlayer stacking, as given by relatively sharp peaks and the enhanced intensities of the obtained diffraction peaks [28]. In

addition, an increased amount of $NaBH_3CN$ results in greater polycondensation and ordered formation of carbon nitride, which is notably noticeable for $SCBCN_{0.4}$, as shown in Fig. S3a. The improved interlayer stacking would facilitate electronic transport, which is predominantly perpendicular to the sheets [29]. By contrast, $SBCN_{0.4}$ demonstrates slightly weakened diffraction peaks ((1 0 0) and (0 0 2)) in Fig. 2a due to the strong reducibility that destroyed or distorted the framework of PCN. Further, the N_2 adsorption-desorption isotherms of all samples presented in Fig. 2b follow the typical type-IV curves with an H3 hysteresis loop, confirming the presence of mesopores. Both two thermal post-treatments increase the pore diameter due to the reductive circumstances (Fig. S4). The detailed BET-specific surface area and pore size distributions of samples were obtained from the adsorption branch and summarized in Table S2, using the BET method and the BJH method, respectively. $SCBCN_{0.4}$ exhibits larger surface areas and enhanced pore structure after modification, which would provide more active sites for the processes of adsorption and photocatalysis. As illustrated in FT-IR spectra (Fig. 2c), pristine PCN displays the typical vibrations of g-C_3N_4 (~3200, 1000–1700, and 810 cm^{-1}), indexed to the stretching vibration of N−H, the stretching vibrations of CN heterocycles, and the bending vibration of heptazine rings, respectively [30]. Distinguished from previous works, the characteristic peak of −C≡N groups (2176 cm^{-1}) emerged while the intensity of N−H stretching vibration enhanced slightly after thermal post-treatment of PCN with $NaBH_3CN$ [31,32]. This could be explained by the presumption that more −C−NH$_2$ groups are generated in the better polycondensation and planar extension than are deprotonated into −C≡N groups. And the −C≡N group formation could be either the result of the deprotonation or the −C≡N source provided by $NaBH_3CN$. Fig. S3b corroborates that the intensities of −C≡N groups steadily enhance as the amount of $NaBH_3CN$ in thermal post-treatment increases, and so do the typical vibrations of g-C_3N_4. The results above signify that $NaBH_3CN$ shows
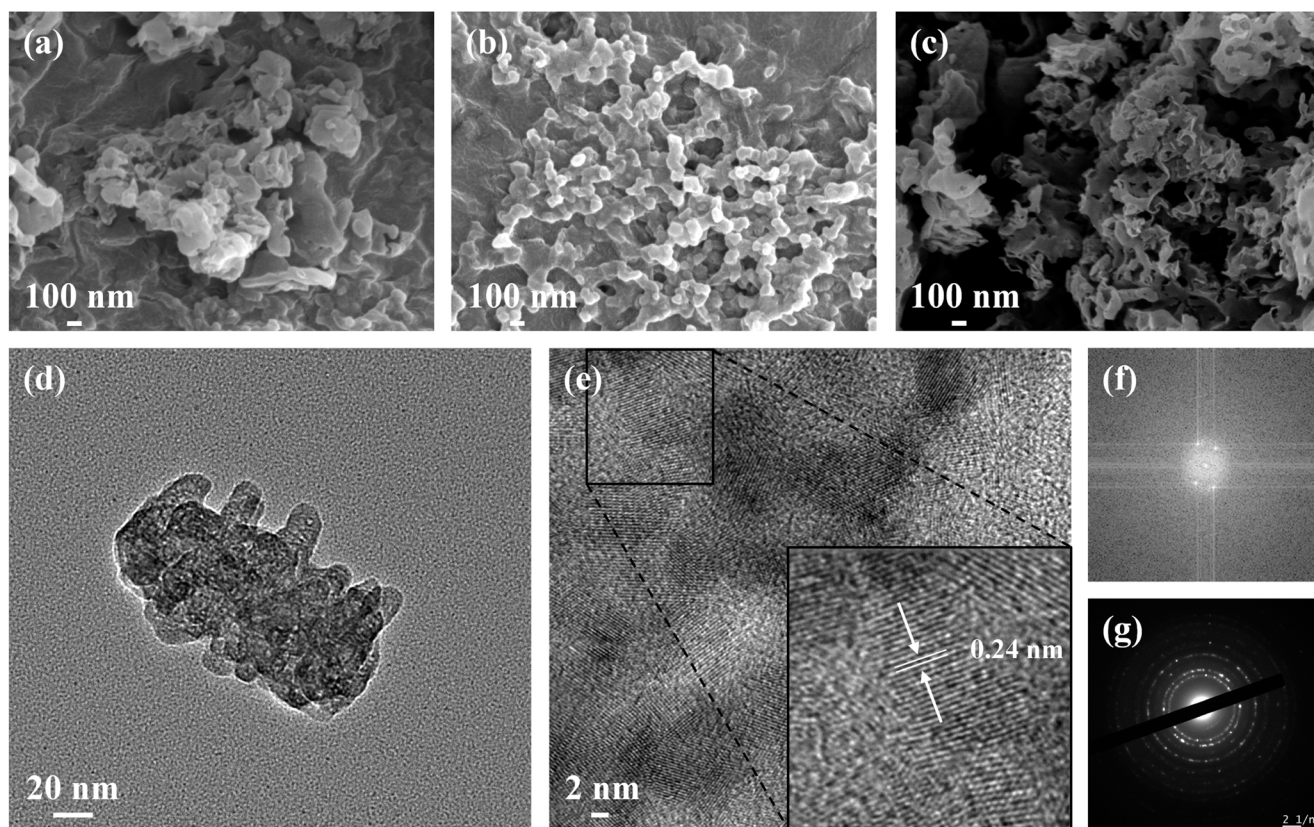

Fig. 1. SEM images of (a) PCN, (b) $SCBCN_{0.4}$, and (c) $SBCN_{0.4}$. (d) TEM image, (e) HRTEM image (High-magnification image inset), and (f) corresponding regional fast Fourier transform pattern of $SCBCN_{0.4}$. (g) SAED image of $SCBCN_{0.4}$.
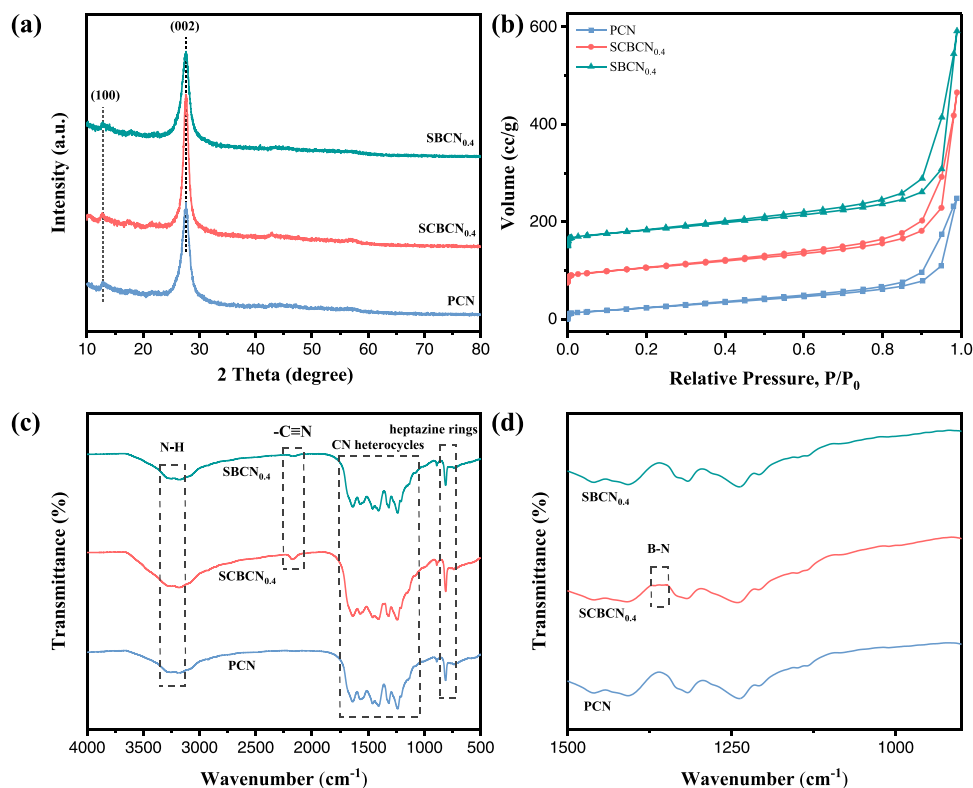
Fig. 2. (a) XRD patterns, (b) N₂ adsorption-desorption isotherms, (c) FT-IR spectra, and (d) corresponding high-magnification FT-IR spectra of PCN, SCBCN$_{0.4}$, and SBCN$_{0.4}$.

unique regulation in introducing defects and improving crystallinity in thermal post-treatment. Furthermore, magnified FT-IR spectra in Fig. 2d manifest that a new peak at around 1356 cm^{-1}, indexed to the stretching vibration of B−N, occurred in SCBCN$_{0.4}$, indicating the doping of B in

the C−N heterocycle [33,34].

The content of C, N, O, and H was investigated using elemental analysis measures. Table S3 reveals that PCN and SBCN$_{0.4}$ have similar element content and N/C atomic ratios (N/C = 1.80). In contrast,
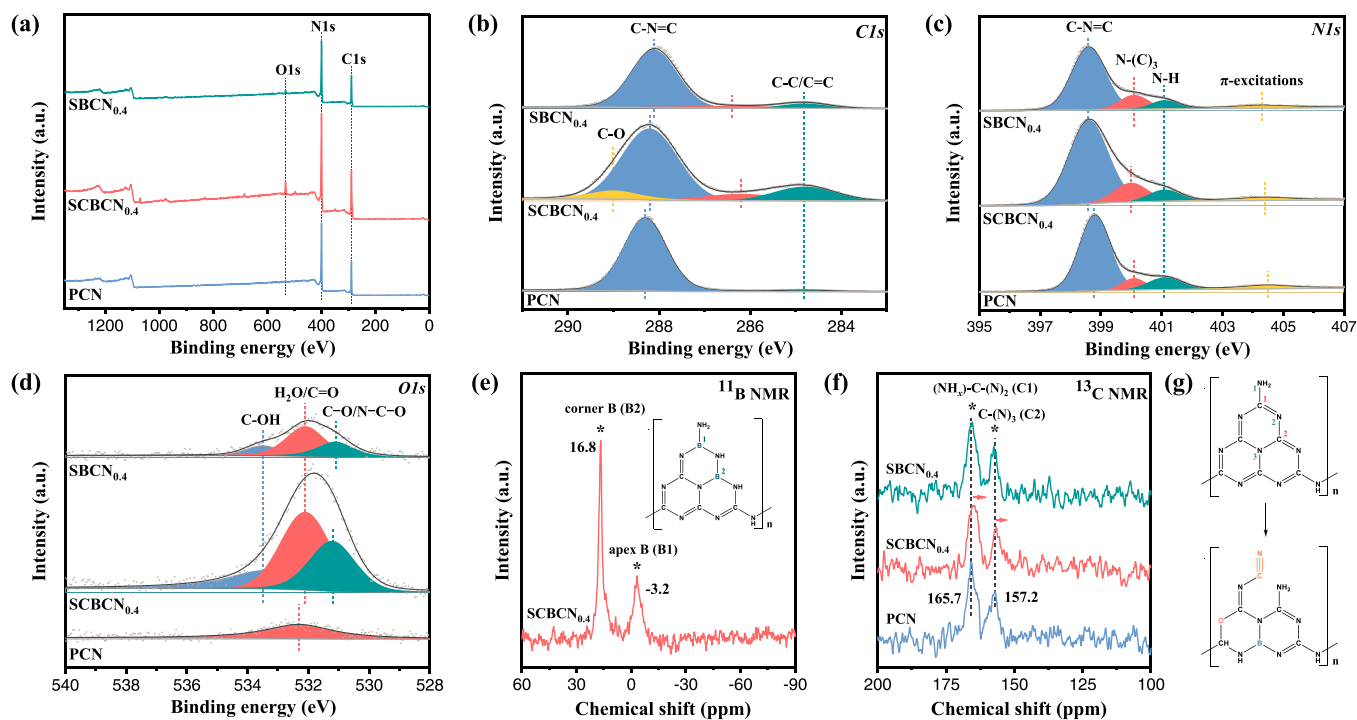

Fig. 3. (a) XPS survey spectra, (b) high-resolution C1s XPS spectra, (c) high-resolution N1s XPS spectra, and (d) high-resolution O1s XPS spectra of PCN, SCBCN$_{0.4}$, and SBCN$_{0.4}$. (e) Solid-state ^{11}B NMR spectrum of SCBCN$_{0.4}$. (f) Solid-state ^{13}C NMR spectrum of PCN, SCBCN$_{0.4}$, and SBCN$_{0.4}$. (g) Proposed structure changes in heptazine units after triple-strategy of modification.

SCBCN$_{0.4}$ has the lowest N/C atomic ratios (N/C = 1.78) and greater O and H contents, suggesting the possible presence of nitrogen vacancies and/or O doping. Moreover, the XPS survey spectra in Fig. 3a and the high-resolution B1s XPS spectra in Fig. S5 also elucidate the elemental composition of samples and the doping of B and O elements in SCBCN$_{0.4}$. As recorded in the high-resolution C1s spectra (Fig. 3b), two distinguishable peaks observed in all samples are assigned to N−C≡N (∼ 288.2 eV) and C−C/C≡C (∼ 284.8 eV) [35]. Notably, the peak situated at around 286.2 eV observed in SCBCN$_{0.4}$ and SBCN$_{0.4}$ might be associated with C−OH or C−O−C or −C≡N or −NH$_x$ (x = 1, 2) groups [2, 31,32,36]. Furthermore, for SCBCN$_{0.4}$, the extra peak centered at the highest binding energy of 289.0 eV implies the new carbon species (C−O/N−C−O) and the successful doping of O atoms by substituting N atoms [37]. Given the relative peak intensity percentages of C1s in Table S4, PCN is mainly composed of tri-s-triazine units, while SCBCN$_{0.4}$ has a higher intensity of (N≡C−N) carbon of the melem framework and moderate dopants. The high-resolution N1s spectra (Fig. 3c) were deconvoluted and showed four distinct peaks at around 398.8, 400.1, 401.1, and 404.4 eV, corresponding to C−N≡C, N−(C)$_3$, −NH$_x$, and π-excitations, respectively [35]. Compared with PCN, SCBCN$_{0.4}$ has higher intensities of C−N≡C (N2) and N−(C)$_3$ (N3), meaning improved crystallinity and planar extension. In the O1s spectra of PCN (Fig. 3d), the peak centered at 532.3 eV might originate from the adsorbed H$_2$O [37]. The O1s spectrum of SCBCN$_{0.4}$ and SBCN$_{0.4}$ were deconvoluted to three peaks: C−O or N−C−O (531.2 eV), adsorbed H$_2$O or C≡O (532.1 eV), and C−OH (533.5 eV) [38]. The results above prove the multi-electron O atoms are embedded into the N-containing aromatic structure and SCBCN$_{0.4}$ has abundant oxygen-containing functional groups (for example, C−OH, C≡O, and COOH). And O atoms prefer to be doped in N2 lattice sites, as testified by the lower peak-area ratio of N2/N3 and the lowest formation energy [39]. The peak at around 192.0 eV in B1s XPS spectra (Fig. S5), assigned to N−B−N bonds, confirms the doping of B in the heptazine rings [18].

Furthermore, the solid-state ^{11}B and ^{13}C NMR measurements were performed to identify the chemical structure and the doping position of

B. Distinguished from previous research, SCBCN$_{0.4}$ presents a more prominent peak at 16.8 ppm and a weaker peak at -3.2 ppm in Fig. 3e, pertaining to the substitution of B at the corner C sites and apex C sites in the tri-s-triazine unit, respectively [33]. And two chemical shifts at around 165.7 and 157.2 ppm, assigned to (NH$_x$)−C−(N)$_2$ (C1) and C−(N)$_3$ (C2), respectively, are observed in the ^{13}C NMR spectrum of all samples in Fig. 3f [40]. No apparent new peak related to the cyano-groups is kept in the ^{13}C NMR of SCBCN$_{0.4}$, which might be explained by the low signal-to-noise ratio. Then, the mildly depressed intensity and the slight shift in (NH$_x$)−C−(N)$_2$ and C−(N)$_3$ of SCBCN$_{0.4}$ in the magnified spectrum reflected the changes in the chemical environment of the C atom (Fig. S6). Relatively significant changes on (NH$_x$)−C−(N)$_2$ are probably due to the incorporation of −C≡N groups in the apex C site [41,42]. And C−(N)$_3$ may be affected by the combined effect of the −C≡N groups and the co-doping of B and O atoms. Thence, the proposed structure changes in heptazine units after the triple-strategy of modification have been demonstrated in Fig. 3g.

As depicted in the UV–Vis diffuse reflectance spectra (UV-DRS) in Fig. 4a, SBCN$_{0.4}$ has an increased UV and visible light response than PCN. In comparison, SCBCN$_{0.4}$ broadens the spectral response range to infrared regions and shows significantly enhanced adsorption in the full spectrum. The bandgap energy (E$_g$) of PCN, SCBCN$_{0.4}$, and SBCN$_{0.4}$ is calculated to be 2.86, 2.85, and 2.94 eV, respectively, according to the Tauc plot (Fig. S7a). The slightly reduced bandgap of SCBCN$_{0.4}$ correlates to a red-shift in the intrinsic absorption band as compared to PCN (Fig. 4a). And the valence band XPS spectra in Fig. S7b demonstrates that the valance band edge potential (E$_{VB}$) of PCN, SCBCN$_{0.4}$, and SBCN$_{0.4}$ is 2.27, 2.35, and 2.18 eV, respectively. A more positive valence band potential of SCBCN$_{0.4}$ indicates a higher oxidation capacity and predictably high-efficiency photocatalytic degradation. Then, the conduction band edge potential (E$_{CB}$) of all samples is obtained as -0.59, -0.50, and -0.76 eV according to the formation that E$_{CB}$ = E$_{VB}$ - E$_g$. Thence, the band positions of all samples concerning NHE at pH = 7.0 are provided in Fig. 4b.

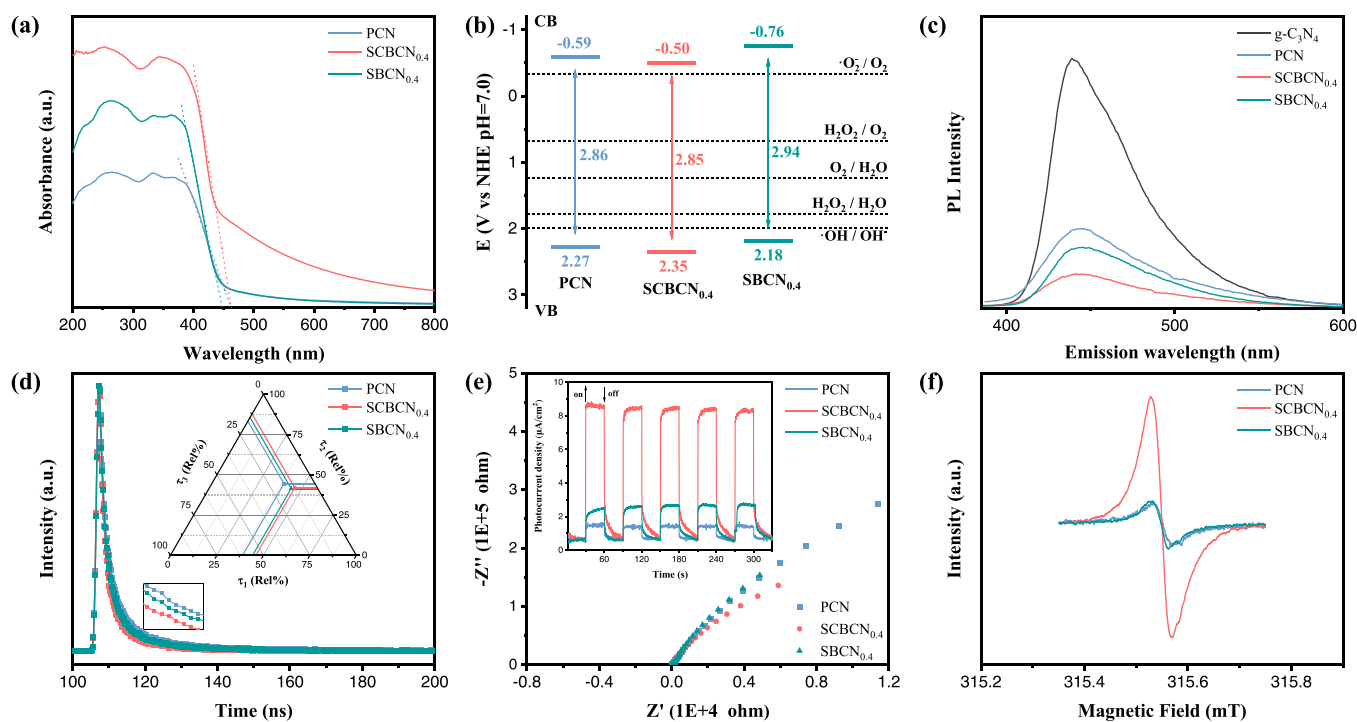Several characterization methods were performed for an insight into

Fig. 4. (a) UV–Vis diffuse reflectance spectra (UV-DRS), (b) bandgap structure, (c) photoluminescence (PL) emission spectra (excited at 367 nm), (d) time-resolved fluorescence decay spectra (excited at 367 nm and monitored at 440 nm), (e) electrochemical impedance spectra (EIS) Nyquist plots (The photocurrent responses cycles insert), and (f) solid electron paramagnetic resonance (EPR) spectra of PCN, SCBCN$_{0.4}$, and SBCN$_{0.4}$.

the efficiency of photogenerated carriers' trapping, separation, migration, and transfer. Compared with other samples, SCBCN$_{0.4}$ has a much quenched PL signal (Fig. 4c), suggesting decreased recombination of photogenerated electron-hole pairs due to the competition for photo-excited charge between the radiative and charge-separating channels [21]. Then, the transient fluorescence decay curves (Fig. 4d) are fitted by the triple-exponential decay function with the value of χ^2 ranging from 1.034 to 1.250, and all parameters are obtained and shown in Table S5. SCBCN$_{0.4}$ presents the fastest tendency of fluorescence decay and depressed average lifetime, signifying the rapid electron transfer and more efficient non-radiative channel, in line with PL spectra [21, 43]. The EIS Nyquist plots in Fig. 4e demonstrate that SCBCN$_{0.4}$ has a lower arc radius of the EIS curve, corroborating a lower interface charge transfer resistance [44]. Further, in several photocurrent response cycles, SCBCN$_{0.4}$ presents six times the photocurrent density of PCN, which is also indicative of the improved separation and transfer of photo-generated carriers. Excellent charge separation and transfer might partly be due to optimization of interlayer perpendicular charge transport induced by improved crystallinity. Furthermore, the −C≡N groups, as strong electron-withdrawing sites, could also contribute to inhibiting the recombination of electron-hole pairs. With differing electronega-tivity and amounts of electrons, doped B and O atoms would promote charge redistribution and operate as exciton dissociation traps, thus improving charge separation. In addition, the solid EPR was investigated to confirm the results above further and detect the vacancy structure of SCBCN$_{0.4}$. As shown in Fig. 4f, all samples exhibit the Lorentzian line, which originates from the delocalized electrons on sp2-carbon atoms of the heptazine rings [45]. SCBCN$_{0.4}$ has a higher signal intensity and concentration of unpaired electrons than other samples, which could be explained by the strong electron-withdrawing effects of −C≡N groups and the regulatory effect of dopants (B and O atoms) on electronic structure and the promotion of unpaired electron formation [17,45].

Density functional theory (DFT) calculations were carried out to elucidate the electron transfer and energy band structure (EBS) evolution of the triple-strategy modified method. According to the structural study of SCBCN$_{0.4}$ above, the −C≡N groups, O doping (N2 sites), and B doping (C2 sites) decorated unit cell of melon-based carbon nitride is illustrated in Fig. 5e, contrasted with the typical structure in Fig. 5a. Then, the bandgap energy of g-C$_3$N$_4$ decreases by 0.13 eV after modi-fication, consistent with the trend observed in DRS spectra. Further-more, the contribution of the density of state (DOS) for g-C$_3$N$_4$ and SCBCN$_{0.4}$ is similar; namely, C 2p and N 2p orbitals contribute compa-rably to CBM (conduction band minimum), while VBM (valence band maximum) is mainly composed of N 2p orbitals. However, the triple-strategy modified method significantly modulates specific energy states, and O and B 2p orbitals also have a non-negligible contribution to CBM and VBM. The partial charge density diagrams show that the molecule orbitals are uniformly delocalized over the heptazine rings in g-C$_3$N$_4$, resulting in a high recombination rate of electron-hole pairs and poor photocatalytic performance [46]. In contrast, triple-strategy modification facilitates the redistribution of charge density and elec-tron transfer, attributed to rich or poor electrons produced by co-dopants and more exciton dissociation traps in SCBCN$_{0.4}$. In short, NaBH$_3$CN-assisted post-treatment enhances directional electron migra-tion while maintaining a high redox capacity, meaning that SCBCN$_{0.4}$ may perform well as a photocatalyst.

3.2. Photocatalytic degradation

The photocatalytic degradation performance of as-prepared photo-catalysts was estimated based on the degradation of DCF and several other pharmaceuticals. Fig. 6a demonstrates that the adsorption of DCF over all photocatalysts before illumination is negligible, and the photolysis of DCF is also ineffective. With the assistance of g-C$_3$N$_4$, PCN, and SBCN$_{0.4}$, about 29%, 81%, and 93% of DCF are degraded within 150 mins, respectively. In contrast, SCBCN$_{0.4}$ completely removes DCF
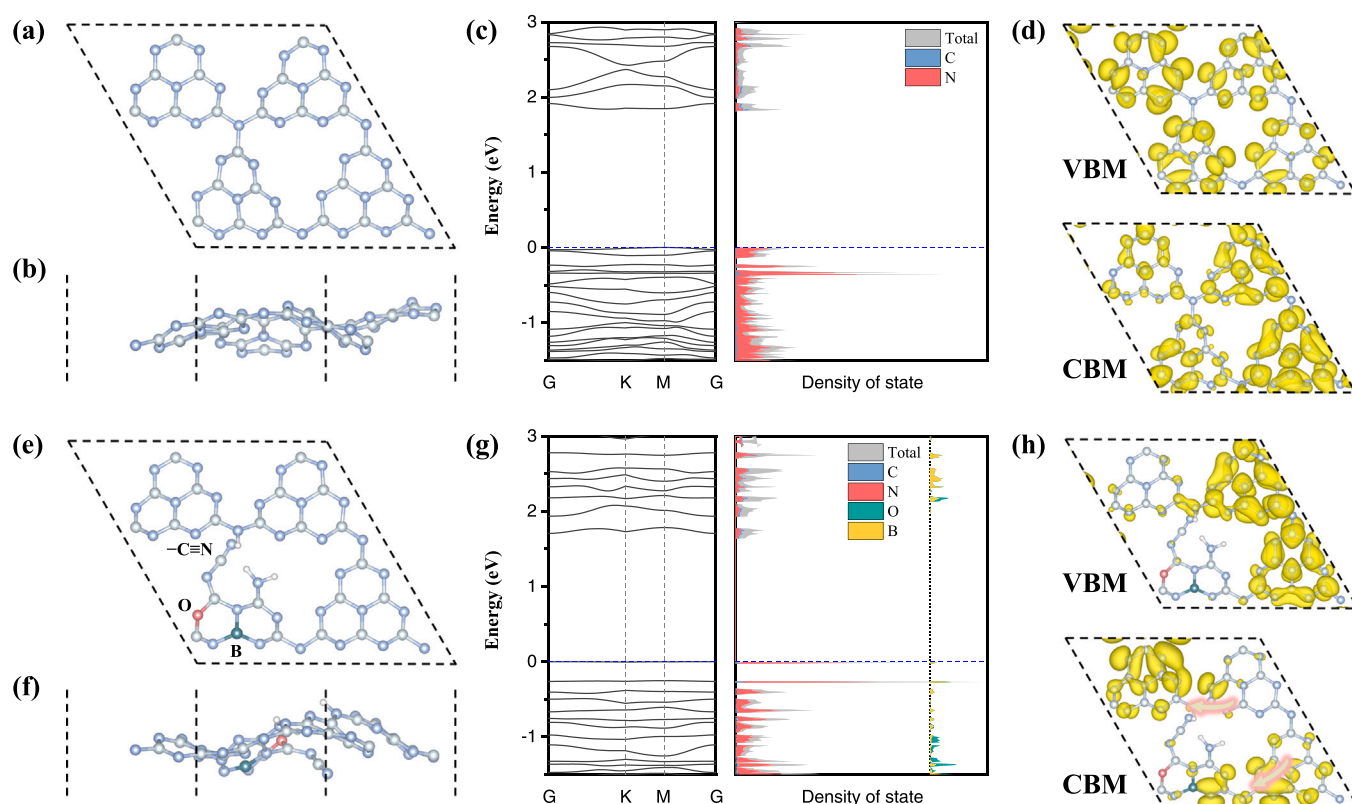

Fig. 5. (a) Top and (b) side view of two-dimensional g-C$_3$N$_4$. (c) EBS, DOS, and (d) partial charge density of g-C$_3$N$_4$. (e) Top and (f) side view of two-dimensional SCBCN$_{0.4}$. (g) EBS, DOS (Corresponding magnified 20 times spectra insert), and (h) partial charge density of SCBCN$_{0.4}$.
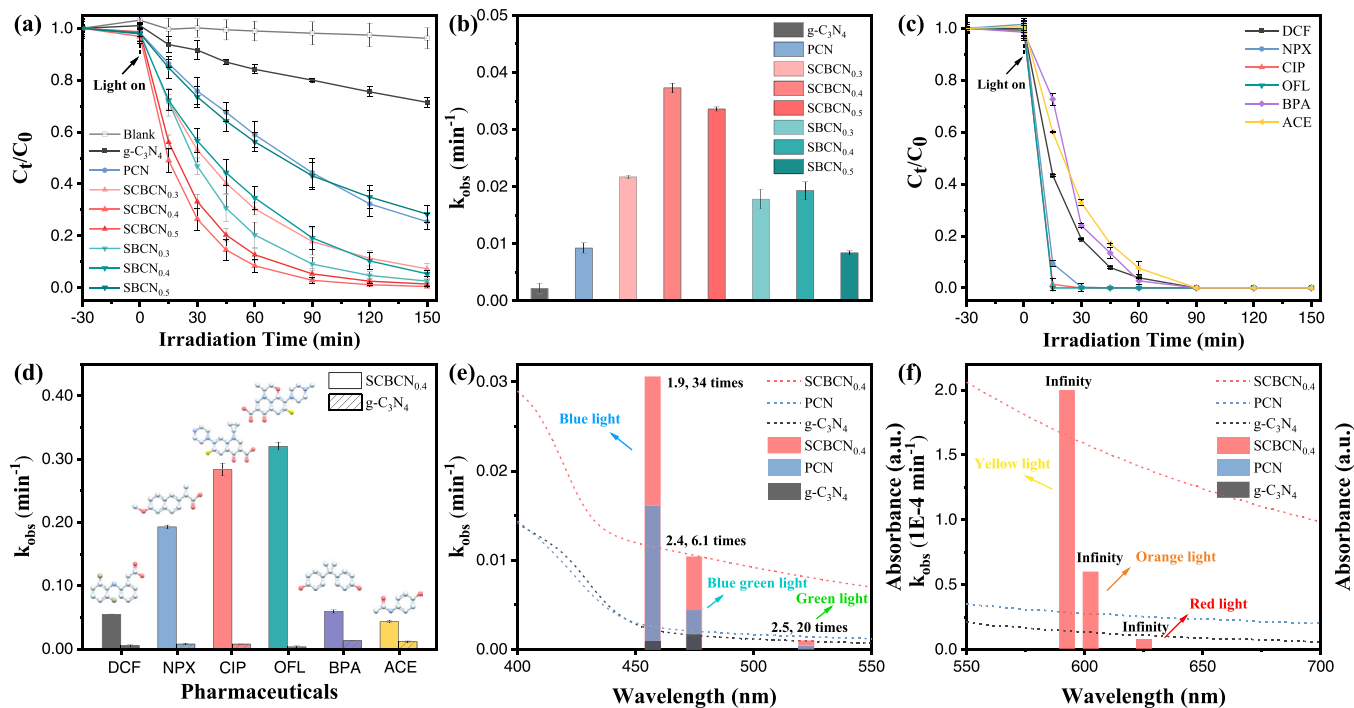
Fig. 6. (a) Kinetic plots and (b) the k_{obs} based on the photocatalytic degradation of DCF over g-C$_3$N$_4$, PCN, SCBCN$_x$, and SBCN$_x$ under visible light irradiation (Initial DCF concentration C$_0$ = 8 mg/L and the catalytic dose is 0.1 g/L). (c) Kinetic plots and (d) the k_{obs} based on the photocatalytic degradation of DCF, NPX, CIP, OFL, BPA, and ACE over SCBCN$_{0.4}$ under visible light irradiation (Initial pharmaceuticals concentration C$_0$ = 2 mg/L and the catalytic dose is 0.1 g/L). UV–Vis diffuse reflectance spectra (Dotted line) and the k_{obs} based on the degradation of DCF over g-C$_3$N$_4$, PCN, and SCBCN$_{0.4}$ under the irradiation of (e) blue light (455–460 nm), blue-green light (470–480 nm), green light (515–530 nm), (f) yellow light (590–590 nm), orange light (600–605 nm), and red light (620–630 nm).

within 90 mins. And the kinetic constant (k_{obs}) of SCBCN$_{0.4}$ (k_{obs} = 0.0373 min^{-1}) is about 17 and 4 times higher than that of g-C$_3$N$_4$ (k_{obs} = 0.0022 min^{-1}) and PCN (k_{obs} = 0.0099 min^{-1}), respectively. As shown in Fig. 6a and b, the amount of NaBH$_4$ and NaBH$_3$CN utilized in the thermal post-treatment, which can modulate crystallinity, −C≡N group strength, and dopant content, also has a substantial impact on photocatalytic performance of SBCN$_x$ and SCBCN$_x$. Fig. S8 also demonstrates that the triple-strategy of modification has a unique promotion on photocatalytic degradation. SCBCN$_{0.4}$ was chosen as the optimum photocatalyst for further experimental investigations. Further, in the photocatalytic degradation of several pharmaceuticals, as shown in Fig. 6c and d, SCBCN$_{0.4}$ exhibits high activity for all tested pollutants. Moreover, the k_{obs} of DCF, naproxen (NPX), ciprofloxacin (CIP), ofloxacin (OFL), bisphenol A (BPA), and acetaminophen (ACE) are about 11, 13, 21, 28, 19, and 16 times higher than that of g-C$_3$N$_4$, respectively. SCBCN$_{0.4}$ shows greater or equivalent increased efficiency in the photocatalytic degradation of several pharmaceuticals, particularly CIP, OFL, and ACE, when compared to most modified g-C$_3$N$_4$ in recent publications (Table S6). In addition, DCF degradation experiments were also carried out under the irradiation of several long-wavelength light sources to confirm the SCBCN$_{0.4}$'s broader spectral response range and photocatalytic performance. As demonstrated in Fig. 6e and Table S7, compared with g-C$_3$N$_4$ and PCN, SCBCN$_{0.4}$ presents improved photocatalytic performance. Under yellow light, orange light, and red light irradiation, no degradation of DCF is observed over g-C$_3$N$_4$ and PCN in Fig. 6f and Table S7, while SCBCN$_{0.4}$ shows weak degradation activity. Namely, SCBCN$_{0.4}$ demonstrates strong light adsorption and high photocatalytic performance in the broad spectrum.

To further evaluate the application potential, the effect of various water quality conditions on the photocatalytic degradation of DCF over SCBCN$_{0.4}$ was investigated, as shown in Fig. S9a–d. SCBCN$_{0.4}$ maintains high degradation activity when the initial pH ranges from 5.0 to 8.0, meaning that it owns a wide pH operation range. Decreasing the initial concentration of DCF from 10 mg/L to 2 mg/L improves the degradation

rate because of the low catalyst loading and significant photon competition at the high initial concentration. The inhibition of the photocatalytic activity by humic acid (HA) presents a positive correlation with HA content. Ionic strength (IS) inhibits DCF degradation, although the inhibition declines when more coexisting NaCl is present. This may be because the quenching impact is gradually counteracted by the solvent cage effect, salting-out effect, and/or the formation of dichloride radicals [47]. Thus, SCBCN$_{0.4}$ still maintains superior performance under water quality conditions.

The scavenger-quenching experiments were performed to identify the generated reactive oxygen species (ROS) and their effects on the photocatalytic process. The photocatalytic reaction rate decreases to varying degrees due to the coexistence of different scavengers (Table S8). As demonstrated in Fig. 7a and b, h$^+$ and ·O$_2^-$ dominate the photocatalytic degradation of DCF over SCBCN$_{0.4}$, while ·OH, e$^-$, and ^{1}O$_2$ also have significant effects in this process. EPR spectra were investigated to elucidate further the ROS generated by as-prepared photocatalysts. And several spin-trapping agents, namely, 5,5-dimethyl-1-pyrroline N-oxide (DMPO), 2,2,6,6-tetramethyl-4-piperidone-N (TEMP), and 2,2,6,6-Tetramethyl-1-piperidinyloxy (TEMPO) were used. Fig. 7c-e illustrate the characteristic signals of DMPO-·OH (1:2:2:1), DMPO-·O$_2^-$ (1:1:1:1), and TEMP-^{1}O$_2$ (1:1:1) adducts respectively, and no obvious signal is detected in darkness [24]. With visible light irradiation, SCBCN$_{0.4}$ generates great ^{1}O$_2$, ·O$_2^-$, and ·OH. Furthermore, the triple signals in Fig. 7f, attributed to TEMPO, would be depressed when TEMPO reacts with e$^-$ or h$^+$ [48]. SCBCN$_{0.4}$ has much-quenched signals of TEMPO, indicating more photogenerated carriers are generated and separated on SCBCN$_{0.4}$. The intermediate products in the photocatalytic degradation of DCF over SCBCN$_{0.4}$ were detected using an UHPLC-Q-Orbitrap and are shown in Table S9. In Fig. S10, the potential DCF degradation pathways and associated ROS are suggested. The mechanism of DCF decomposition includes hydroxylation, dehydration, dehydrogenation, decarbonylation, decarboxylation, dechlorination, amide bond cleavage, aldehyde reaction, and
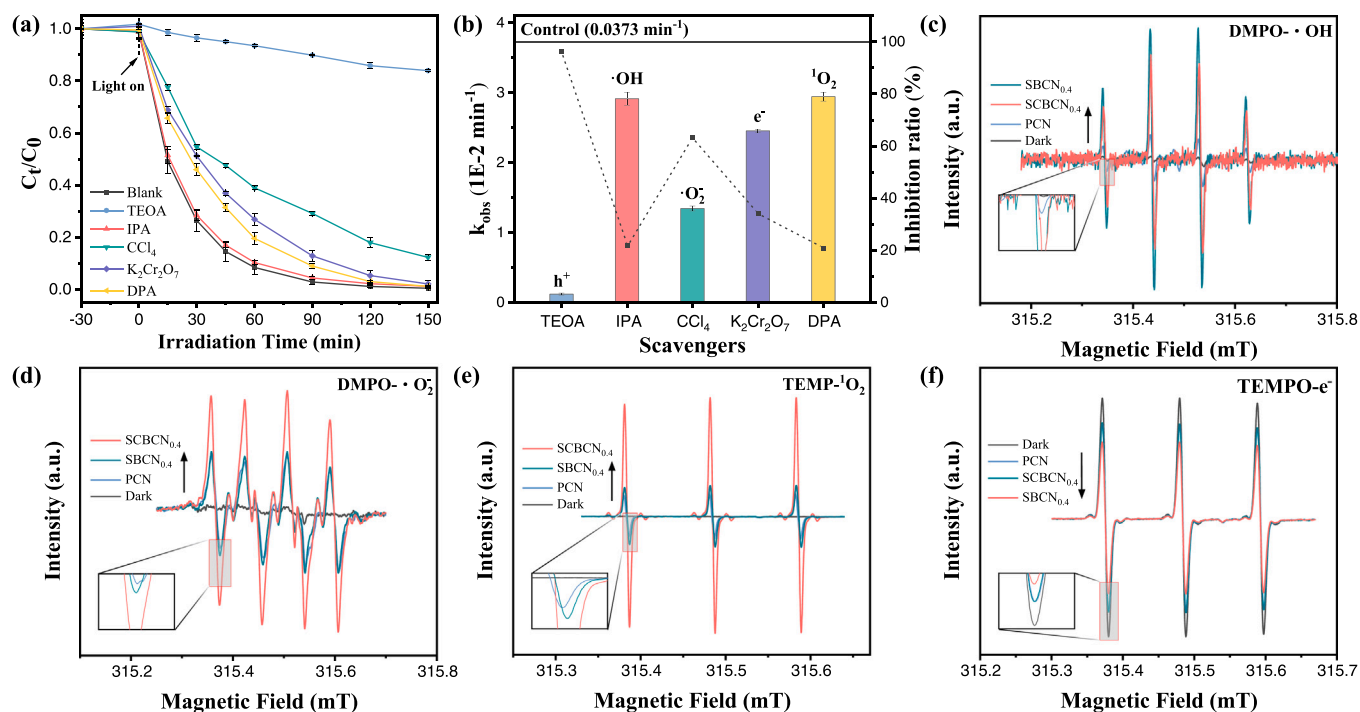
Fig. 7. (a) Kinetic plots and (b) the k_{obs} based on the effects of several scavengers on the degradation of DCF over SCBCN$_{0.4}$ (The dotted line serves only to emphasize the comparison and has no actual significance). EPR spectra of as-prepared photocatalysts with (c) DMPO in H_2O, (d) DMPO in methanol, (e) TEMP in H_2O, and (f) TEMPO in H_2O.

formylation. ROS are necessary for the degradation pathways that would further attack and mineralize intermediates.

3.3. Photocatalytic H_2O_2 production

The photocatalytic H_2O_2 production by as-prepared photocatalysts was carried out to further evaluate photocatalytic performance. Fig. 8a shows that pristine g-C$_3$N$_4$ produces 30.59 μmol/L H_2O_2 within 1 hour
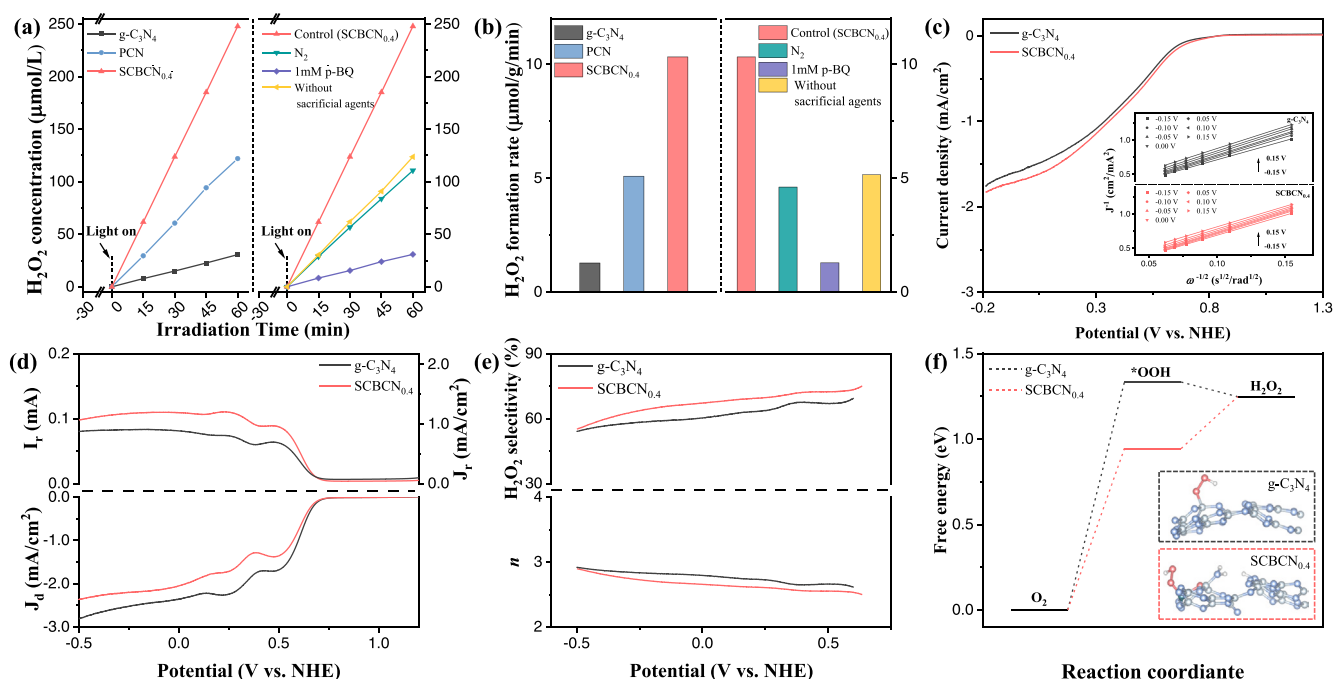

Fig. 8. (a) Time profiles and (b) formation rate of the photocatalytic H_2O_2 production over g-C$_3$N$_4$, PCN, SCBCN$_{0.4}$ (O_2 atmospheres, 10 vol% ethanol), and SCBCN$_{0.4}$ under several conditions. (c) Linear sweep voltammetry (LSV) curves of the g-C$_3$N$_4$ and SCBCN$_{0.4}$ measured on RDE at 1600 rpm (Koutecky-Levich plots insert). (d) LSV curves of g-C$_3$N$_4$ and SCBCN$_{0.4}$ recorded on an RRDE with a 5 mV/s scan rate and a rotating rate of 1600 rpm, together with the detected H_2O_2 currents on the ring electrode (upper panel) at a fixed potential of 1.2 V vs. RHE. (e) Calculated H_2O_2 selectivity and electron transfer number (n) during LSV scan. (f) Calculated Gibbs free energy diagrams for the 2e$^-$ oxygen reduction reaction (ORR) over g-C$_3$N$_4$ and SCBCN$_{0.4}$.

of visible light irradiation. In contrast, $SCBCN_{0.4}$ exhibits a superior H_2O_2 production performance (247.83 μmol/L) under the same conditions, and the H_2O_2 formation rate is about 8.10 times higher than that of pristine g-C_3N_4. As shown in Table S10, $SCBCN_{0.4}$ presents a higher H_2O_2 formation rate and/or improved efficiency than most various modified g-C_3N_4 in recent publications. Furthermore, under nitrogen purging conditions (Fig. S12), $SCBCN_{0.4}$ produces 110.63 μmol/L H_2O_2 within 1 hour, indicating that water oxidation reaction (WOR, Eq. (1)) is also an essential mechanism for H_2O_2 production in this system [10]. Then, with the consumption of $\cdot O_2^-$ by p-benzoquinone (p-BQ), the photocatalytic H_2O_2 evolution over $SCBCN_{0.4}$ has been inhibited. Thus, the synthesis of H_2O_2 over the conduction band of $SBCN_{0.4}$ is more via an indirect sequential two-step single-electron reduction route (Eqs. (2) and (3)) than the direct one-step two-electron reduction route (Eq. (4)) [9]. In addition, $SCBCN_{0.4}$ also shows the great potential of H_2O_2 production (309 μmol/g/h) in the absence of sacrificial agents, which is superior to most various modified g-C_3N_4 and metal-free photocatalysts reported so far (Table S10) [49].

$$2H_2O + 2h^+ \rightarrow H_2O_2 + 2H^+ \tag{1}$$

$$O_2 + e^- \rightarrow \cdot O_2^- \tag{2}$$

$$\cdot O_2^- + 2H^+ + e^- \rightarrow H_2O_2 \tag{3}$$

$$O_2 + 2H^+ + 2e^- \rightarrow H_2O_2 \tag{4}$$

The ORR activity was evaluated by rotating disk electrode (RDE) and rotating ring disk electrode (RRDE) measurements. g-C_3N_4 and $SCBCN_{0.4}$ have similar current profiles at different rotating speeds (Fig. S13a and b), and the current becomes stronger as the speed increases. Noted that $SCBCN_{0.4}$ has higher limited current density and onset potential at 1600 rpm (Fig. 8c). The average electron transfer numbers (n) of g-C_3N_4 (1.40) and $SCBCN_{0.4}$ (1.43) obtained by the Koutecky-Levich equation (Fig. 8c and Table S11) illustrate that the two-electron transfer pathway may dominate the O_2-to-H_2O_2 conversion and $SCBCN_{0.4}$ has great selectivity. The polarization curve of g-C_3N_4 and $SCBCN_{0.4}$, as well as the related H_2O_2 generation current, have been demonstrated in Fig. 8d. In terms of O_2 reduction and H_2O_2 generation, $SCBCN_{0.4}$ outperforms g-C_3N_4 [50]. And the improved ORR activity of $SCBCN_{0.4}$ is further substantiated by a slight positive shift in onset potential (defined as the potential at the current density of 0.1 mA·cm^{-2}) and the change in relevant Tafel slopes (Fig. S13c) [51]. Then, H_2O_2 selectivity and electron transfer number (n) are plotted as functions of applied potential and are displayed in Fig. 8e, where $SCBCN_{0.4}$ exhibits better H_2O_2 selectivity, reaching a maximal H_2O_2 selectivity of more

than 75% within the tested applied potential range. High activity and selectivity for photocatalytic H_2O_2 production on $SCBCN_{0.4}$ might be due in part to the promotion of $-C\equiv N$ groups for *OOH formation and subsequent hydrogenation [15,16]. Then, abundant oxygen-containing functional groups on $SCBCN_{0.4}$ can also promote $2e^-$ ORR through adjusting the adsorption and binding of O_2 and intermediates or activating adjacent carbon atoms [52,53]. Meanwhile, doped B and O atoms could facilitate O_2 adsorption and protonation while lowering the energy barrier, resulting in high H_2O_2 production and selectivity [19,20]. The DFT calculations also confirmed that the calculated adsorption energy of *OOH significantly decreased after modification (from 0.48 eV to 0.05 eV, Fig. S13d and e), and the Gibbs free energy of intermediate *OOH formation is much lower at $SCBCN_{0.4}$ than g-C_3N_4 (Fig. 8f).

3.4. Photocatalytic mechanism

The investigation above revealed that $SCBCN_{0.4}$ exhibits significantly improved photocatalytic performance, and Scheme 1 illustrates specific photocatalytic processes that were suggested.

$SCBCN_{0.4}$ has a broader spectral response range and better light-harvesting ability in full spectrum, culminating in more charge carrier excitation. Then, decoration of $-C\equiv N$ defects, B atoms, and O atoms would serve as exciton dissociation traps for capturing photoexcited electrons and enhancing directional electron migration. Besides that, optimization of interlayer stacking facilitates electron perpendicular transport, and doped B and O atoms would promote charge redistribution and enhance the delocalized conjugated π system. Because $SCBCN_{0.4}$ has a greater surface area and a superior pore structure, there are more active sites for adsorption and photocatalysis. For photocatalytic degradation, the more positive valence band potential of $SCBCN_{0.4}$ promotes the generation of high-oxidation holes and the abatement of DCF molecules. What's more, the abundance of separated electrons and holes could produce $\cdot O_2^-$, $^1O_2$, and $\cdot OH$, along with efficiently decomposing DCF. For photocatalytic H_2O_2 production, separated electrons and holes on $SCBCN_{0.4}$ would undergo synchronous ORR and WOR. Specifically, separated electrons would reduce O_2 and produce H_2O_2 primarily via an indirect sequential two-step single-electron reduction route but also via a direct one-step two-electron reduction route. And separated holes could directly oxidize H_2O molecules into H_2O_2 via a two-electron water oxidation pathway. The $-C\equiv N$ defects, oxygen-containing functional groups, and doped B and O atoms could facilitate higher activity and selectivity of photocatalytic H_2O_2 production through the synergistic effect.
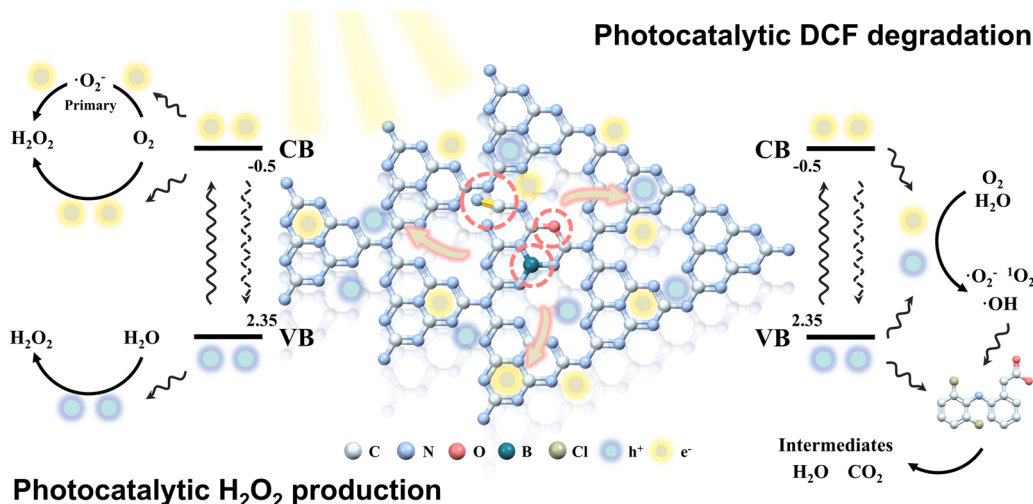
Scheme 1. Photocatalytic mechanism of DCF degradation and H_2O_2 production over $SCBCN_{0.4}$.

3.5. Detoxification, reusability, and stability evaluation

According to the acute toxicity tests shown in Fig. S14a, the inhibition ratio of luminescent bacteria (*Photobacterium phoshoreum T3 spp.*) presents an overall downward trend with irradiation time. Furthermore, Fig. S14b demonstrates that the recurring photocatalytic degradation of DCF has only a minor decrease in activity. And $SCBCN_{0.4}$ also exhibits the excellent reusability of $SCBCN_{0.4}$ in cycling runs for photocatalytic H_2O_2 production, as shown in Fig. S15a and b. After photocatalytic experiments, XRD and FT-IR spectra in Fig. S16a and b reflect that $SCBCN_{0.4}$ retains its intact structure. Thence, $SCBCN_{0.4}$ exhibits high detoxification, cycling stability, and persistent photocatalytic activity, which means a practical application potential in environmental remediation.

4. Conclusion

In summary, the triple-strategy of modification increases crystallinity while also decorating moderate $-C\equiv N$ defects, B atoms, and O atoms in modified $g-C_3N_4$ ($SCBCN_{0.4}$) by the thermal post-treatment of self-assembled carbon nitride with sodium cyanoborohydride. The novel $NaBH_3CN$-assisted post-treatment shows unique regulatory effects on microstructure, electronic structure, light-harvesting capability, as well as carrier transfer efficiency. Benefiting from the multiple advantages above, $SCBCN_{0.4}$ has exceptional DCF degrading performance even when exposed to long-wavelength light and the effects of diverse water quality conditions. $SCBCN_{0.4}$ exhibits high activities for all tested pharmaceuticals, especially CIP, OFL, and ACE, which is superior to all modified $g-C_3N_4$ reported so far. Moreover, $SCBCN_{0.4}$ exhibits a high in-situ photocatalytic H_2O_2 production rate of 620 μmol/g/h via synchronous oxygen reduction and water oxidation reactions, as well as up to 309 μmol/g/h in pure water, indicating $SCBCN_{0.4}$ outperforms most modified $g-C_3N_4$ and metal-free photocatalysts. Due to the moderate $-C\equiv N$ defects, oxygen-containing functional groups, and B and O co-dopants, $SCBCN_{0.4}$ has a maximal H_2O_2 selectivity of over 75% and higher activity for H_2O_2 production via a two-electron transfer process. Furthermore, $SCBCN_{0.4}$'s excellent detoxification, reusability, and stability were validated in several experiments. Therefore, this research offers a ground-breaking approach to manufacturing triple-strategy modified $g-C_3N_4$ for environmental remediation and (sacrificial-free) in-situ H_2O_2 production.

CRediT authorship contribution statement

Qinglun You: Conceptualization, Methodology, Investigation, Data curation, Visualization, Writing – original draft, Writing – review & editing. **Chunsheng Zhang:** Investigation, Data curation. **Min Cao:** Investigation, Data curation, Software. **Bin Wang:** Resources, Funding acquisition. **Jun Huang:** Resources, Funding acquisition. **Yujue Wang:** Resources, Funding acquisition. **Shubo Deng:** Resources, Funding acquisition. **Gang Yu:** Resources, Writing – review & editing, Funding acquisition.

Declaration of Competing Interest

The authors declare that they have no known competing financial interests or personal relationships that could have appeared to influence the work reported in this paper.

Data availability

Data will be made available on request.

Acknowledgment

Appendix A. Supplementary material

Supplementary data associated with this article can be found in the online version at doi:10.1016/j.apcatb.2022.121941.

References

[1] G. Wu, J. Geng, Y. Shi, L. Wang, K. Xu, H. Ren, Comparison of diclofenac transformation in enriched nitrifying sludge and heterotrophic sludge: transformation rate, pathway, and role exploration, Water Res. 184 (2020), 116158.

[2] H. Zind, L. Mondamert, Q.B. Remaury, A. Cleon, N.K.V.E.L. Leitner, J. Labanowski, Occurrence of carbamazepine, diclofenac, and their related metabolites and transformation products in a French aquatic environment and preliminary risk assessment, Water Res. 196 (2021), 117052.

[3] P. Sathishkumar, K. Mohan, R.A.A. Meena, M. Balasubramanian, L. Chitra, A. R. Ganesan, T. Palvannan, S.K. Brar, F.L. Gu, Hazardous impact of diclofenac on mammalian system: mitigation strategy through green remediation approach, J. Hazard. Mater. 419 (2021), 126135.

[4] J.M. Brozinski, M. Lahti, A. Meierjohann, A. Oikari, L. Kronberg, The anti-inflammatory drugs diclofenac, naproxen and ibuprofen are found in the bile of wild fish caught downstream of a wastewater treatment plant, Environ. Sci. Technol. 47 (2013) 342–348.

[5] H. Guo, Z. Xu, D. Wang, S. Chen, D. Qiao, D. Wan, H. Xu, W. Yan, X. Jin, Evaluation of diclofenac degradation effect in "active" and "non-active" anodes: a new consideration about mineralization inclination, Chemosphere 286 (2022), 131580.

[6] Y. Liu, Y. Zhao, J. Wang, Fenton/Fenton-like processes with in-situ production of hydrogen peroxide/hydroxyl radical for degradation of emerging contaminants: advances and prospects, J. Hazard. Mater. 404 (2021), 124191.

[7] J.M. Campos-Martin, G. Blanco-Brieva, J.L.G. Fierro, Hydrogen peroxide synthesis: an outlook beyond the anthraquinone process, Angew. Chem. Int. Ed. 45 (2006) 6962–6984.

[8] L. Li, Z. Hu, J.C. Yu, On-demand synthesis of H_2O_2 by water oxidation for sustainable resource production and organic pollutant degradation, Angew. Chem. Int. Ed. 59 (2020) 20538–20544.

[9] H. Hou, X. Zeng, X. Zhang, Production of hydrogen peroxide by photocatalytic processes, Angew. Chem. Int. Ed. 59 (2020) 17356–17376.

[10] J. Zhang, J. Lang, Y. Wei, Q. Zheng, L. Liu, Y.-H. Hu, B. Zhou, C. Yuan, M. Long, Efficient photocatalytic H_2O_2 production from oxygen and pure water over graphitic carbon nitride decorated by oxidative red phosphorus, Appl. Catal. B 298 (2021), 120522.

[11] J. Liu, Y. Liu, N. Liu, Y. Han, X. Zhang, H. Huang, Y. Lifshitz, S.T. Lee, J. Zhong, Z. Kang, Metal-free efficient photocatalyst for stable visible water splitting via a two-electron pathway, Science 347 (2015) 970–974.

[12] S. Gao, X. Wang, C. Song, S. Zhou, F. Yang, Y. Kong, Engineering carbon-defects on ultrathin $g-C_3N_4$ allows one-pot output and dramatically boosts photoredox catalytic activity, Appl. Catal. B 295 (2021), 120272.

[13] A. Kumar, V. Krishnan, Vacancy engineering in semiconductor photocatalysts: implications in hydrogen evolution and nitrogen fixation applications, Adv. Funct. Mater. 31 (2021) 2009807.

[14] W. Yang, L. Zhang, J. Xie, X. Zhang, Q. Liu, T. Yao, S. Wei, Q. Zhang, Y. Xie, Enhanced photoexcited carrier separation in oxygen-doped $ZnIn_2S_4$ nanosheets for hydrogen evolution, Angew. Chem. Int. Ed. 55 (2016) 6716–6720.

[15] L. Chen, C. Chen, Z. Yang, S. Li, C. Chu, B. Chen, Simultaneously tuning band structure and oxygen reduction pathway toward high-efficient photocatalytic hydrogen peroxide production using cyano-rich graphitic carbon nitride, Adv. Funct. Mater. 31 (2021) 2105731.

[16] X. Zhang, P. Ma, C. Wang, L. Gan, X. Chen, P. Zhang, Y. Wang, H. Li, L. Wang, X. Zhou, K. Zheng, Unraveling the dual defect sites in graphite carbon nitride for ultra-high photocatalytic H_2O_2 evolution, Energy Environ. Sci. 15 (2022) 830–842.

[17] Y. Gao, Y. Zhu, L. Lyu, Q. Zeng, X. Xing, C. Hu, Electronic structure modulation of graphitic carbon nitride by oxygen doping for enhanced catalytic degradation of organic pollutants through peroxymonosulfate activation, Environ. Sci. Technol. 52 (2018) 14371–14380.

[18] Z. Wang, M. Chen, Y. Huang, X. Shi, Y. Zhang, T. Huang, J. Cao, W. Ho, S.C. Lee, Self-assembly synthesis of boron-doped graphitic carbon nitride hollow tubes for enhanced photocatalytic NO_x removal under visible light, Appl. Catal. B 239 (2018) 352–361.

[19] Y. Xia, X. Zhao, C. Xia, Z.Y. Wu, P. Zhu, J.Y. Kim, X. Bai, G. Gao, Y. Hu, J. Zhong, Y. Liu, H. Wang, Highly active and selective oxygen reduction to H_2O_2 on boron-doped carbon for high production rates, Nat. Commun. 12 (2021) 4225.

[20] R. Du, K. Xiao, B. Li, X. Han, C. Zhang, X. Wang, Y. Zuo, P. Guardia, J. Li, J. Chen, J. Arbiol, A. Cabot, Controlled oxygen doping in highly dispersed Ni-loaded $g-C_3N_4$ nanotubes for efficient photocatalytic H_2O_2 production, Chem. Eng. J. 441 (2022), 135999.

[21] Y. Guo, J. Li, Y. Yuan, L. Li, M. Zhang, C. Zhou, Z. Lin, A rapid microwave-assisted thermolysis route to highly crystalline carbon nitrides for efficient hydrogen generation, Angew. Chem. Int. Ed. 55 (2016) 14693–14697.

[22] H. Yu, H. Ma, X. Wu, X. Wang, J. Fan, J. Yu, One-step realization of crystallization and cyano-group generation for g-C₃N₄ photocatalysts with improved H₂ production, Sol. RRL 5 (2021) 2000372.

[23] X. Chen, R. Shi, Q. Chen, Z. Zhang, W. Jiang, Y. Zhu, T. Zhang, Three-dimensional porous g-C₃N₄ for highly efficient photocatalytic overall water splitting, Nano Energy 59 (2019) 644–650.

[24] Q. You, Q. Zhang, M. Gu, R. Du, P. Chen, J. Huang, Y. Wang, S. Deng, G. Yu, Self-assembled graphitic carbon nitride regulated by carbon quantum dots with optimized electronic band structure for enhanced photocatalytic degradation of diclofenac, Chem. Eng. J. 431 (2022), 133927.

[25] J. Cao, J. Zhang, Xa Dong, H. Fu, X. Zhang, X. Lv, Y. Li, G. Jiang, Defective borate-decorated polymer carbon nitride: enhanced photocatalytic NO removal, synergy effect and reaction pathway, Appl. Catal. B 249 (2019) 266–274.

[26] M. Zhang, L. He, T. Shi, R. Zha, Neat 3D C₃N₄ monolithic aerogels embedded with carbon aerogels via ring-opening polymerization with high photoreactivity, Appl. Catal. B 266 (2020), 118652.

[27] S. Yang, Y. Gong, J. Zhang, L. Zhan, L. Ma, Z. Fang, R. Vajtai, X. Wang, P. M. Ajayan, Exfoliated graphitic carbon nitride nanosheets as efficient catalysts for hydrogen evolution under visible light, Adv. Mater. 25 (2013) 2452–2456.

[28] J. Liao, W. Cui, J. Li, J. Sheng, H. Wang, X. Dong, P. Chen, G. Jiang, Z. Wang, F. Dong, Nitrogen defect structure and NO⁺ intermediate promoted photocatalytic NO removal on H₂ treated g-C₃N₄, Chem. Eng. J. 379 (2020), 122282.

[29] C. Merschjann, S. Tschierlei, T. Tyborski, K. Kailasam, S. Orthmann, D. Hollmann, T. Schedel-Niedrig, A. Thomas, S. Lochbrunner, Complementing graphenes: 1D interplanar charge transport in polymeric graphitic carbon nitrides, Adv. Mater. 27 (2015) 7993–7999.

[30] J. Jiang, D. Duan, J. Ma, Y. Jiang, R. Long, C. Gao, Y. Xiong, Van der waals heterostructures by single cobalt sites-anchored graphene and g-C₃N₄ nanosheets for photocatalytic syngas production with tunable CO/H₂ ratio, Appl. Catal. B 295 (2021) 120261.

[31] X. Hu, P. Lu, R. Pan, Y. Li, J. Bai, Y. He, C. Zhang, F. Jia, M. Fu, Metal-ion-assisted construction of cyano group defects in g-C₃N₄ to simultaneously degrade wastewater and produce hydrogen, Chem. Eng. J. 423 (2021) 130278.

[32] J. Liu, Z. Wei, W. Fang, Z. Jiang, W. Shangguan, Enhanced photocatalytic hydrogen evolution of the hydrogenated deficient g-C₃N₄ via surface hydrotreating, ChemCatChem 11 (2019) 6275–6281.

[33] Y. Wang, H. Li, J. Yao, X. Wang, M. Antonietti, Synthesis of boron doped polymeric carbon nitride solids and their use as metal-free catalysts for aliphatic C-H bond oxidation, Chem. Sci. 2 (2011) 446–450.

[34] X. Zeng, H. Chen, X. He, H. Zhang, W. Fang, X. Du, W. Li, Z. Huang, L. Zhao, In-situ synthesis of non-phase-separated boron carbon nitride for photocatalytic reduction of CO₂, Environ. Res. (2021) 112178.

[35] B. Ma, G. Chen, C. Fave, L. Chen, R. Kuriki, K. Maeda, O. Ishitani, T.C. Lau, J. Bonin, M. Robert, Efficient visible-light-driven CO₂ reduction by a cobalt molecular catalyst covalently linked to mesoporous carbon nitride, J. Am. Chem. Soc. 142 (2020) 6188–6195.

[36] F. Wang, Y. Wang, Y. Feng, Y. Zeng, Z. Xie, Q. Zhang, Y. Su, P. Chen, Y. Liu, K. Yao, W. Lv, G. Liu, Novel ternary photocatalyst of single atom-dispersed silver and carbon quantum dots co-loaded with ultrathin g-C₃N₄ for broad spectrum photocatalytic degradation of naproxen, Appl. Catal. B 221 (2018) 510–520.

[37] S. Samanta, R. Yadav, A. Kumar, A. Kumar Sinha, R. Srivastava, Surface modified C, O co-doped polymeric g-C₃N₄ as an efficient photocatalyst for visible light assisted CO₂ reduction and H₂O₂ production, Appl. Catal. B 259 (2019) 118054.

[38] Y. Zhou, J. Jiang, Y. Gao, J. Ma, S.-Y. Pang, J. Li, X.-T. Lu, L.-P. Yuan, Activation of peroxymonosulfate by benzoquinone: a novel nonradical oxidation process, Environ. Sci. Technol. 49 (2015) 12941–12950.

[39] Z.-F. Huang, J. Song, L. Pan, Z. Wang, X. Zhang, J.-J. Zou, W. Mi, X. Zhang, L. Wang, Carbon nitride with simultaneous porous network and O-doping for efficient solar-energy-driven hydrogen evolution, Nano Energy 12 (2015) 646–656.

[40] Y. Qin, J. Lu, X. Zhao, X. Lin, Y. Hao, P. Huo, M. Meng, Y. Yan, Nitrogen defect engineering and π-conjugation structure decorated g-C₃N₄ with highly enhanced visible-light photocatalytic hydrogen evolution and mechanism insight, Chem. Eng. J. 425 (2021), 131844.

[41] H. Yu, R. Shi, Y. Zhao, T. Bian, Y. Zhao, C. Zhou, G.I.N. Waterhouse, L.Z. Wu, C. H. Tung, T. Zhang, Alkali-assisted synthesis of nitrogen deficient graphitic carbon nitride with tunable band structures for efficient visible-light-driven hydrogen evolution, Adv. Mater. 29 (2017) 1605148.

[42] D. Zhao, C.L. Dong, B. Wang, C. Chen, Y.C. Huang, Z. Diao, S. Li, L. Guo, S. Shen, Synergy of dopants and defects in graphitic carbon nitride with exceptionally modulated band structures for efficient photocatalytic oxygen evolution, Adv. Mater. 31 (2019) 1903545.

[43] M.Q. Yang, Y.J. Xu, W. Lu, K. Zeng, H. Zhu, Q.H. Xu, G.W. Ho, Self-surface charge exfoliation and electrostatically coordinated 2D hetero-layered hybrids, Nat. Commun. 8 (2017) 14224.

[44] Y. Xu, M. Fan, W. Yang, Y. Xiao, L. Zeng, X. Wu, Q. Xu, C. Su, Q. He, Homogeneous carbon/potassium-incorporation strategy for synthesizing red polymeric carbon nitride capable of near-infrared photocatalytic H₂ production, Adv. Mater. 33 (2021) 2101455.

[45] W. Wang, H. Zhang, S. Zhang, Y. Liu, G. Wang, C. Sun, H. Zhao, Potassium-ion-assisted regeneration of active cyano groups in carbon nitride nanoribbons: visible-light-driven photocatalytic nitrogen reduction, Angew. Chem. Int. Ed. 58 (2019) 16644–16650.

[46] B. Zhu, L. Zhang, B. Cheng, J. Yu, First-principle calculation study of tri-s-triazine-based g-C₃N₄: A review, Appl. Catal. B 224 (2018) 983–999.

[47] J. Fu, G.Z. Kyzas, Z. Cai, E.A. Deliyanni, W. Liu, D. Zhao, Photocatalytic degradation of phenanthrene by graphite oxide-TiO₂-Sr(OH)₂/SrCO₃ nanocomposite under solar irradiation: effects of water quality parameters and predictive modeling, Chem. Eng. J. 335 (2018) 290–300.

[48] J. Gao, F. Zhang, H. Xue, L. Zhang, Y. Peng, X. Li, Y. Gao, N. Li, G. Lei, In-situ synthesis of novel ternary CdS/PdAg/g-C₃N₄ hybrid photocatalyst with significantly enhanced hydrogen production activity and catalytic mechanism exploration, Appl. Catal. B 281 (2021), 119509.

[49] L. Zhou, J. Lei, F. Wang, L. Wang, M.R. Hoffmann, Y. Liu, S.-I. In, J. Zhang, Carbon nitride nanotubes with in situ grafted hydroxyl groups for highly efficient spontaneous H₂O₂ production, Appl. Catal. B 288 (2021), 119993.

[50] K. Jiang, S. Back, A.J. Akey, C. Xia, Y. Hu, W. Liang, D. Schaak, E. Stavitski, J. K. Nørskov, S. Siahrostami, H. Wang, Highly selective oxygen reduction to hydrogen peroxide on transition metal single atom coordination, Nat. Commun. 10 (2019) 3997.

[51] B. Liu, J. Du, G. Ke, B. Jia, Y. Huang, H. He, Y. Zhou, Z. Zou, Boosting O₂ reduction and H₂O dehydrogenation kinetics: surface N-Hydroxymethylation of g-C₃N₄ photocatalysts for the efficient production of H₂O₂, Adv. Funct. Mater. 32 (2022) 2111125.

[52] K.-H. Wu, D. Wang, X. Lu, X. Zhang, Z. Xie, Y. Liu, B.-J. Su, J.-M. Chen, D.-S. Su, W. Qi, S. Guo, Highly selective hydrogen peroxide electrosynthesis on carbon: In situ interface engineering with surfactants, Chem 6 (2020) 1443–1458.

[53] Z. Lu, G. Chen, S. Siahrostami, Z. Chen, K. Liu, J. Xie, L. Liao, T. Wu, D. Lin, Y. Liu, T.F. Jaramillo, J.K. Nørskov, Y. Cui, High-efficiency oxygen reduction to hydrogen peroxide catalysed by oxidized carbon materials, Nat. Catal. 1 (2018) 156–162.